Complete composition tunability of InGaN nanowires using a combinatorial approach

TEVYE KUYKENDALL[1], PHILIPP ULRICH[1], SHAUL ALONI[2] AND PEIDONG YANG[1,2]*

[1]Department of Chemistry, University of California, Berkeley, California 94720, USA

[2]Molecular Foundry, Materials Science Division, Lawrence Berkeley National Laboratory, Berkeley, California 94720, USA

*e-mail: p_yang@berkeley.edu

Published online: 28 October 2007; doi:10.1038/nmat2037

The III nitrides have been intensely studied in recent years because of their huge potential for everything from high-efficiency solid-state lighting and photovoltaics to high-power and temperature electronics[1–3]. In particular, the InGaN ternary alloy is of interest for solid-state lighting and photovoltaics because of the ability to tune the direct bandgap of this material from the near-ultraviolet to the near-infrared region. In an effort to synthesize InGaN nitride, researchers have tried many growth techniques[4–13]. Nonetheless, there remains considerable difficulty in making high-quality InGaN films and/or freestanding nanowires with tunability across the entire range of compositions. Here we report for the first time the growth of single-crystalline $In_xGa_{1-x}N$ nanowires across the entire compositional range from $x = 0$ to 1; the nanowires were synthesized by low-temperature halide chemical vapour deposition[9] and were shown to have tunable emission from the near-ultraviolet to the near-infrared region. We propose that the exceptional composition tunability is due to the low process temperature and the ability of the nanowire morphology to accommodate strain-relaxed growth[14], which suppresses the tendency toward phase separation that plagues the thin-film community.

Although much progress has been made in the synthesis of high-quality films by metal–organic chemical vapour deposition (MOCVD)[4–7], molecular beam epitaxy[8,14] and hydride vapour-phase epitaxy[12,13], all of these methods still must contend with the lack of native substrates for epitaxy, which leads to threading dislocations in the InGaN and GaN layers due to lattice mismatch. On the other hand, the unique growth mechanism of nanowires[15] has been shown to all but eliminate threading dislocations, which usually act as non-radiative recombination centres[16,17]. This may be essential for overcoming the so-called 'valley of death' drop-off in PL efficiency for high-In-concentration samples[18,19]. Although some progress has been made in incorporating indium into gallium nitride nanowires using MOCVD, this has been primarily in the form of thin-film cladding of GaN wires[20] or the introduction of quantum wells within GaN wires[21]. Hydride vapour-phase epitaxy has been shown to be one of the most promising methods for making $In_xGa_{1-x}N$ nanowires so far[22]; however, this method has been limited to a maximum indium incorporation of $x = 0.2$ owing to the excess hydrogen evolved as a product of the reaction of HCl with the metal In and Ga precursors. Hydrogen is well known to affect the indium incorporation in InGaN alloys[23,24]. Another issue for most growth methods is the difficulty of nitrogen incorporation, particularly for In-rich nitride alloys, which has led to the need for increasingly high ammonia flow rates. In the low-temperature halide chemical vapour deposition approach reported here, drop-off in PL efficiency for high-In-concentration samples seems to be minimal, excess hydrogen is limited to that introduced by ammonia and a relatively low V–III ratio is found to be necessary. In addition, the use of chloride precursors eliminates the issue of carbon contamination encountered for MOCVD.

The synthesis was carried out using a simple, yet effective, reactor design shown in Fig. 1. Four temperature zones were created using a horizontal, single-zone tube furnace and two independently controlled heating elements. $InCl_3$, $GaCl_3$ and NH_3 were used as the In, Ga and N sources respectively. Nitrogen carrier gas was used to transport the $InCl_3$ and $GaCl_3$ precursors separately through two of the inner tubes, whereas NH_3 was carried through the third inner tube and allowed to mix at the position of the substrate shown on the right. The synthesis requires no catalyst and can be carried out on a variety of substrates. Thin Si or sapphire substrate strips were placed perpendicular to the outlets, along isothermal lines, such that the composition and corresponding properties of the nanowires were a result of the precursor-mixing gradient. Although a temperature gradient of $\sim 50\,^{\circ}C$ was present over the range covered by the substrates, little difference in wire morphology and/or other properties was observed as a result. The composition gradient was sharp close to the outlets and tended to spread with increasing distance downstream of the outlets.

On cooling, the substrates were observed to have a matte finish and a variety of colours ranging from clear to light yellow on the GaN side to reddish-black on the InN side (Fig. 1, inset). Figure 2a (sample 1–13) shows scanning electron microscopy (SEM, see also Supplementary Information, Fig. S1) images of the nanowires grown on a silicon substrate from GaN (Fig. 2a, sample 1) to InN (Fig. 2a, sample 13). Towards the Ga-rich side, the nanowires are tapered and have diameters and lengths of 10–50 nm and 0.5–1 μm, respectively. The wires grow more sharply tapered, with a widening base, at an indium concentration between 70 and 90%, and to a larger, less tapered, morphology between 90 and 100%. The indium-rich wires have diameters and lengths of 100–250 nm and 1–2 μm, respectively.

Figure 2b shows X-ray diffraction (XRD) patterns of wires at several positions (samples 1–13) along the compositional gradient. The XRD patterns indicate that the wires have the wurtzite crystal structure. The peaks correspond to the (100), (002) and (101) planes from left to right, and the plots are ordered with increasing indium concentration from 1 to 13. The absence of multiple sets of

© 2007 Nature Publishing Group

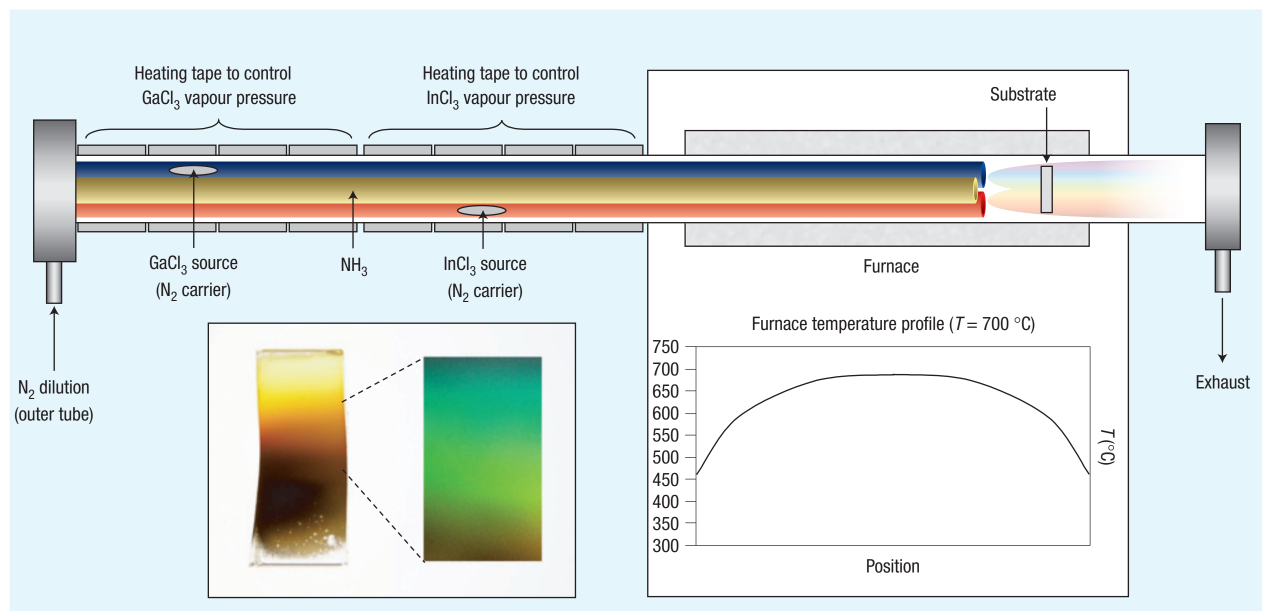

Figure 1 Experimental set-up. The reactor consists of three inner quartz tubes, which supply the reactive gases, $InCl_3$, $GaCl_3$ (N_2 carrier) and NH_3, and an outer quartz tube, which supplies inert gas (N_2) and houses the reaction in a horizontal tube furnace. Two independently controlled heating tapes were used to tune the vapour pressure of the $InCl_3$ and $GaCl_3$ precursors. The positioning of the reactive gas outlets results in the observed InGaN compositional gradient. Shown below the furnace is the temperature profile, indicating that the centre of the furnace is maintained at 700 °C, whereas the substrates are at ∼550 °C. Inset: Photograph of an as-made sample on quartz (left) and a colour image from PL of a section of substrate (right).

peaks, as seen by other authors[25], indicates that the wires are not phase separated. However, some extent of composition modulation was indeed observed by transmission electron microscopy (TEM) for samples with 70–90% In, and will be discussed later. The full-width at half-maximum of the 002 peak is $2\theta = 0.34°$ and 0.44° for InN and GaN respectively and reaches a maximum of 0.96° around 50% indium. For comparison, the full-width at half-maximum for high-quality GaN thin films is around 0.17° (ref. 26). This broadening might arise from several factors[27], such as the distribution of bond lengths for a random alloy[28], size-dependent broadening and the large size of the X-ray beam spot across the composition gradient. Figure 2c shows the lattice constants a and c, determined from XRD, plotted as a function of the indium concentration. The indium concentration was obtained with a scanning electron microscope by energy-dispersive X-ray spectroscopy (EDS). The red and blue lines show the Vegard-law approximation of the a and c lattice constants as a function of indium concentration using the values of $a = 3.189$ Å and 3.535 Å and $c = 5.188$ Å and 5.709 Å for GaN and InN respectively. This plot shows a near-linear relationship between the lattice spacing and the alloy composition.

TEM analysis of these wires indicates that the wires are single crystalline. Figure 3 shows the electron-diffraction patterns and phase-contrast images of wires at ∼20% increments. The electron-diffraction patterns indicate the single-crystal nature of the wires. The wires were shown to grow along the [002] direction. The electron-diffraction patterns show the 002 diffraction and clearly demonstrate the change in (002) lattice spacing as a function of indium concentration. Green dashed lines are drawn over the electron-diffraction images as a reference for comparison of the spacing. The compositions shown in the figure were determined by TEM-EDS. The phase-contrast images also indicate the crystalline nature of the wires. Lack of large variations in contrast indicates that there are no large variations in the indium concentrations or phase segregation in the wires. In the region of concentrations between 70 and 90% In, however, there was some compositional modulation[14] that can be seen in the TEM image. Some texturing was also observed in this range of compositions. Many authors suggest that at the temperature used here there is a miscibility gap over most of the compositional range from ∼5 to 90% In, and over the rest of this range the metastable state is formed[29,30]. Although the extent of the metastable region has not been determined, we do not observe the predicted miscibility gap in our growth process. It has been reported that increased indium incorporation can occur owing to the onset of 'strain relaxed growth'[14,31]. For epitaxially grown GaN/InGaN thin films, this occurs at a critical thickness following a pseudomorphically strained layer. The nanowire morphology is expected to enhance strain relaxation[17]. With the results for the InGaN nanowires grown here, we observe high indium mole fractions with little or no pseudomorphic layer or phase separation. Finally, nanowire growth is possibly enabled by the self-catalysed process that we observed previously for GaN (ref. 32). We believe the low temperature (∼550 °C) and high growth rate[32] promote the formation of the non-thermodynamically-stable product.

The optical properties of the nanowires were characterized by several techniques and the results clearly demonstrate a shift in bandgap as a function of composition. Figure 4 shows room-temperature CCD (charge-coupled device) images, photoluminescence (PL) emission spectra, absorption spectra and energy gap plotted as a function of composition. The colour CCD images (Fig. 4a), showing the emission when pumped with a continuous-wave 325 nm HeCd laser, were taken at regular intervals along the substrate and show the vibrant colours emitted by the sample at wavelengths in the visible region of the spectrum. Across the samples, a near continuum of colours from the intermediate

© 2007 Nature Publishing Group

compositions was observed (Fig. 1, inset). Figure 4b shows the PL intensity of the $In_xGa_{1-x}N$ nanowires plotted as a function of wavelength from 325 to 850 nm. The peaks shift to longer wavelengths with increasing indium concentration x. Some defect emission is observed at lower indium concentrations. Importantly, although the PL intensities are normalized in this plot, it is worth noting that, when corrected for the wavelength-dependent absorption of the glass microscope optics, the optical fibre and the detector efficiency, the emission peak intensities vary within a factor of ~1.7 for $x = 0$ to 0.6. The corrected relative peak intensities are plotted as a function of wavelength in Fig. 4c. It is interesting to note that the commonly observed 'valley of death' drop-off in PL efficiency observed for high-indium-concentration MOCVD samples seems to be significantly diminished for these InGaN nanowires. In addition, it has been shown that the presence of spontaneous polarization in GaN has a drastic impact on electron–hole overlap, radiative lifetimes and subsequent emission wavelength and quantum efficiencies for GaN (ref. 33). The development of low-dimensional wurtzite InGaN nanostructures here is expected to provide an interesting material platform to explore such an effect in the alloyed InGaN system[15,33]. Figure 4d shows the optical absorption spectrum for the nanowires, plotted as a function of photon energy. The absorption edge also shifts systematically to lower energy as x increases.

Figure 4e shows the PL peak energy, and the bandgap determined collectively by optical absorption and electron energy loss spectroscopy (EELS), plotted as a function of composition x. The EELS bandgap measurement was taken on single wires using TEM, and serves to confirm the values measured by PL emission and optical absorption, as well as to confirm that the bandgap shift is due to individual wires of varying composition and not any possible underlying thin film. The compositions were determined by SEM-EDS for the PL emission and optical absorption measurements, and by TEM-EDS for the EELS measurement. The red line in Fig. 4e shows the bowing parameter of the bandgap obtained by optical absorption as a function of composition. The data were fitted by the following standard bowing equation:

$$F(x) = P_1(1-x) + P_2x - Bx(1-x),$$

where $F(x)$ is the energy gap as a function of composition x. P_1 and P_2 represent the bandgaps at $x = 0$ and $x = 1$ respectively, and B is the bowing parameter. The following values were obtained: GaN, $P_1 = 3.43$ eV; InN, $P_2 = 1.12$ eV; $B = 1.01$ eV. The value for pure GaN is well accepted as the true bandgap for this material, whereas that of InN falls somewhere in the middle of the disputed range of values for this material between 0.7 eV and 1.9 eV (refs 34,35). Although much of the more recent literature is leaning towards the 0.7 eV value, a proposed explanation of the disparate results is that there is a dependence of the bandgap on the free-electron concentration[35]. This model would indicate an approximate free-electron concentration of $n = 10^{20}$ cm^{-3} for our InN sample. The small bowing parameter agrees well with the more recent literature on the subject[8,30].

Using chloride precursors and a combinatorial synthetic approach, we have demonstrated the ability to tune the composition and energy gap (from the near-ultraviolet to the near-infrared region) of single-crystalline InGaN nanowires across the entire alloy range. We have demonstrated the exceptional optical properties of these nanowires as both ensemble arrays and single wires by PL, absorption and EELS spectroscopy. Taken together, this represents the most complete collection of bandgap determination as a function of concentration from a single synthetic source. It demonstrates that, all other synthetic parameters being equal, there is a smooth dependence of the bandgap on composition from GaN to InN. In contrast to most MOCVD thin-film InGaN studies, no obvious 'valley of death' drop-off in PL efficiency for high-indium-concentration samples was observed for these nanowires. These nanowires could be used in applications such as solid-state lighting as well as solar-energy conversion.

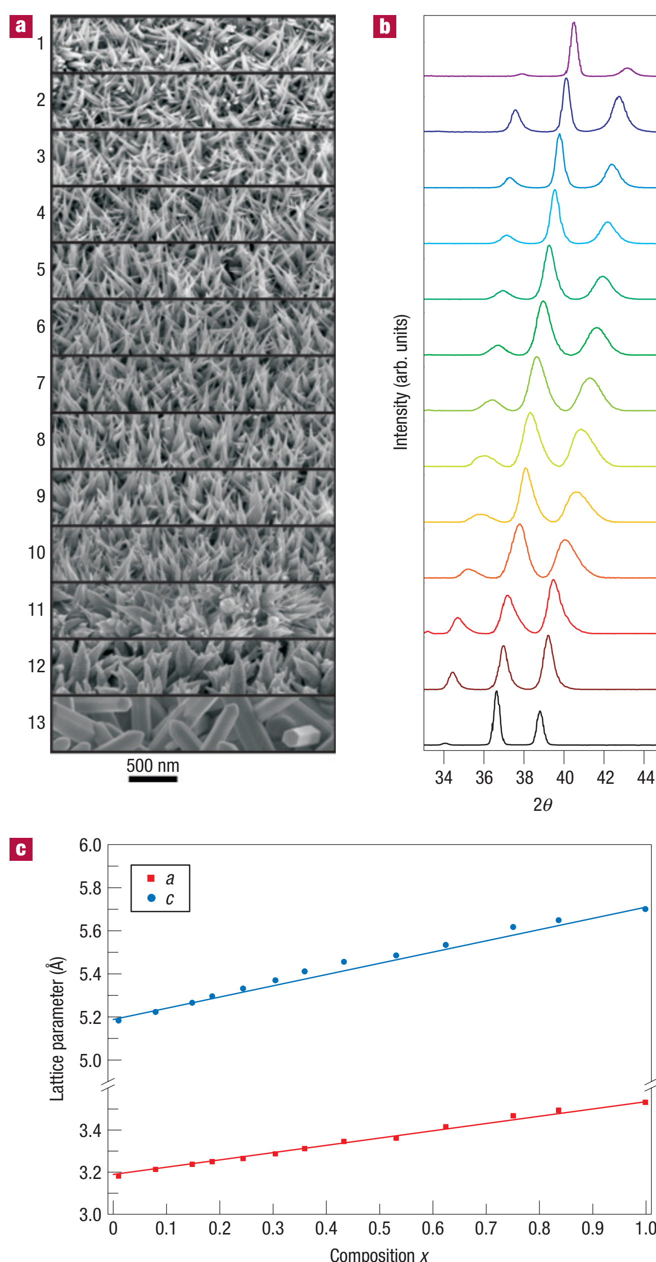

Figure 2 Wire morphology and XRD at varying InGaN composition. a, SEM images of the nanowire morphology, with increasing In concentration from images 1 to 13. The wire morphology changes most noticeably in 10–11 from the smaller to larger wires at around 75–90% In. **b**, 100, 002 and 101 XRD peaks from left to right of the nanowires, with increasing In concentration from images 1 to 13. **c**, Lattice constants *a* and *c* derived from the 100 and 002 diffraction peaks respectively, plotted as a function of In concentration determined by EDS, and Vegard-law values for the respective *a* and *c* lattice constants as a function of indium concentration (red and blue lines).

© 2007 Nature Publishing Group

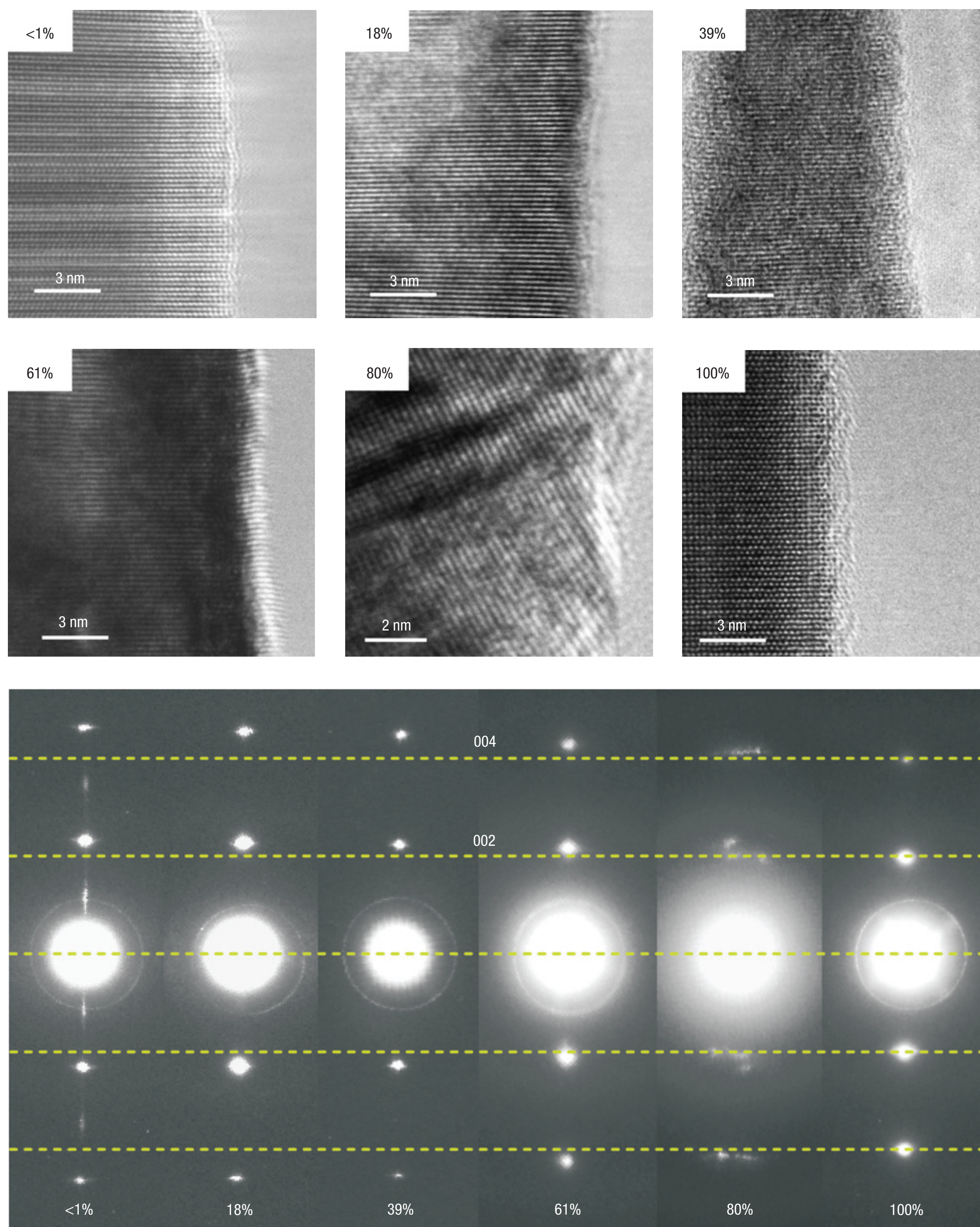

Figure 3 TEM characterization of the InGaN nanowires. Phase-contrast TEM images (top) and electron-diffraction images (bottom) of InGaN nanowires, with percentage indium indicated.

METHODS

SYNTHESIS

Three 1/4″-diameter quartz (inner) tubes were placed inside a 1″-diameter quartz (outer) tube for the transport of $InCl_3$, $GaCl_3$ and NH_3 to the reaction zone. Alfa Aesar 5N pure anhydrous $InCl_3$ and 5N pure ultradry $GaCl_3$ were packed inside one of each of the inner tubes and sandwiched by two tufts of quartz wool. The tubes were filled inside a glove box, and remained sealed during transfer to the system. Nitrogen was used as the $InCl_3$ and $GaCl_3$ carrier gas, at a flow rate of 10 sccm. The $GaCl_3$ and $InCl_3$ precursors were heated to 50–60 °C and 390–410 °C respectively. The third inner tube carried NH_3 at a flow rate of 100 sccm. The tubes were stacked in a tripod configuration and

© 2007 Nature Publishing Group

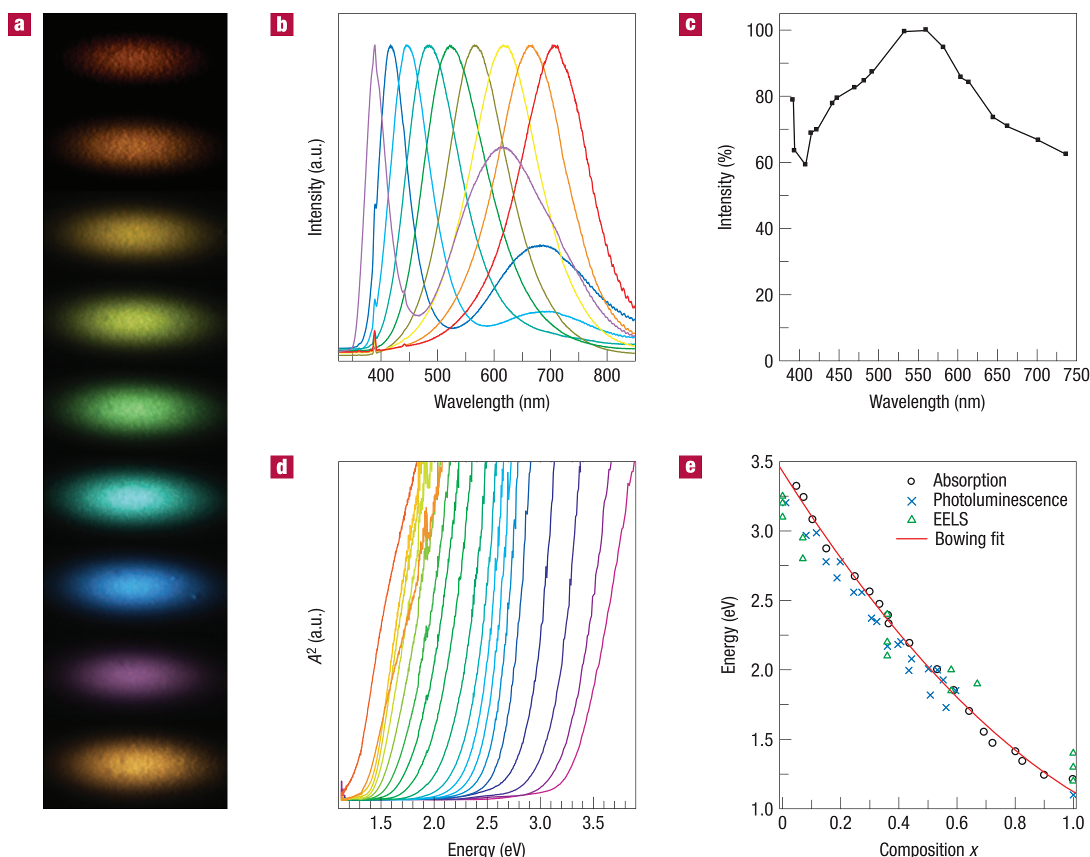

Figure 4 Optical characterization of the InGaN nanowires. a, Colour CCD images, **b**, visible PL emission ($x = 0$–0.6), **c**, corrected peak intensities and **d**, optical absorption spectra ($x = 0$–1.0) of the $In_xGa_{1-x}N$ nanowire arrays taken at intervals across the substrates with varying concentration x. **e**, Energy plotted as a function of In concentration x determined by EDS for PL, absorption and EELS and bowing equation fit to absorption spectra.

positioned so that the outlets were in the appropriate temperature region of the furnace. The substrates (Si(111), sapphire or quartz) were sonicated in acetone, cleaned with DI water and isopropanol and placed on a quartz plank 0–2 cm downstream from the outlets. The substrate temperatures were in the 575−525 °C range. The temperature at the centre of the furnace was 700 °C. The outer tube contained nitrogen at a flow rate of 300 sccm for purging and reactant dilution. The reactions were carried out at atmospheric pressure.

CHARACTERIZATION

TEM images were collected with a Phillips CM200/FEG (field-emission gun) microscope at 200 kV, equipped with a Link EDS detector. The nanowires were dispersed on amorphous holey-carbon-coated Cu grids.

XRD spectra were collected on a Bruker-AXS D8 with a general area detector diffraction system and Co Kα radiation (1.79026 Å). The substrate containing the (as-prepared) InGaN nanowires was placed onto the sample holder while focusing a 0.5 mm beam on regions of nanowires at regular intervals along the substrate.

SEM and EDS were taken using a JEOL JSM-6340F field-emission scanning electron microscope equipped with a Genesis energy-dispersive X-ray analysis detector. The spectra were collected from a ∼108 μm^2 area, at an accelerating voltage of 20 kV. To correlate the composition determined by EDS with the properties determined by XRD, PL and optical absorption, the substrate was accurately positioned using the x–y translation stage, and the locations were recorded. The background-subtracted In L and Ga K lines were analysed using the energy-dispersive X-ray analysis software's standardless-quantification mode, and have an error of ±∼2%.

The PL spectra were collected with a Nikon microscope, equipped with a 50× objective, output to a multimode fibre-optic cable, dispersed by a 250 grooves mm^{-1} optical grating and detected with a liquid-N_2-cooled silicon CCD. The sample was irradiated using a 325 nm continuous-wave HeCd laser with a 5 mW unpolarized beam that was focused to a spot size of ∼50 μm × 100 μm. The PL data for near-infrared samples are not included in this report owing to large instrumental uncertainty in our micro-PL set-up.

Optical absorption spectra were collected using an Agilent 8453 ultraviolet–visible spectrometer. The spectrometer was equipped with a Custom Sensors and Technology 9001B fibre-optic coupler to focus and collect light from a small area. The sample was illuminated with a ∼1-mm-diameter spot using the bare fibre, and collected with a collimator attached to a second fibre. Wire arrays were grown on quartz substrates for optical transparency. The energy gap was fitted by linear extrapolation from a plot of the absorption squared as a function of bandgap.

The high-energy-resolution EELS bandgap determination in combination with Z-contrast imaging was carried out using an FEI Tecnai F20 UT microscope operated at 200 kV equipped with a double-focusing Wien filter acting as a monochromator directly below the field-emission gun. This set-up in combination with a high-resolution Gatan imaging filter (GIF) and an improved high-voltage supply allows for a ∼2-nm-sized electron probe with an energy resolution, defined by the full-width at half-maximum of the zero-loss peak, of ∼0.2 eV. The low-loss region of the electron energy-loss spectra is thus hardly affected by the broad tails of the zero-loss peak, the signal to background ratio in the low-loss region is enhanced and the low-loss electron energy-loss information can unambiguously be accessed down to about 0.7 eV. As the InGaN alloys are direct-bandgap semiconductors, a sharp onset in the loss spectra is expected at the bandgap energy. The bandgap value has been defined by two methods once the zero-loss peak contribution has been subtracted from the acquired data. The first method defines the bandgap as the inflection point in the loss curve. The second method is a result of a fitting the data to a power law $(E - E_g)^n$, where $n = 0.5$ for direct-bandgap semiconductors. The latter defines the onset of the bandgap absorption whereas the inflection point is more sensitive to the energy resolution, thus $E_{PL} \approx E_{IP} - 0.5 \cdot \mathrm{FWHM}$.

© 2007 Nature Publishing Group

Received 15 June 2007; accepted 21 September 2007; published 28 October 2007.

References

1. Schubert, E. F. & Kim, J. K. Solid-state light sources getting smart. *Science* **308**, 1274–1278 (2005).
2. Wu, J. *et al.* Superior radiation resistance of $In_{1-x}Ga_xN$ alloys: Full-solar-spectrum photovoltaic material system. *J. Appl. Phys.* **94**, 6477–6482 (2003).
3. Kung, P. & Razeghi, M. III-Nitride wide bandgap semiconductors: A survey of the current status and future trends of the material and device technology. *Opto-Electron. Rev.* **8**, 201–239 (2000).
4. Schenk, H. P. D. *et al.* Indium incorporation above 800 °C during metalorganic vapor phase epitaxy of InGaN. *Appl. Phys. Lett.* **75**, 2587–2589 (1999).
5. Shan, W. *et al.* Optical properties of $In_xGa_{1-x}N$ alloys grown by metalorganic chemical vapor deposition. *J. Appl. Phys.* **84**, 4452–4458 (1998).
6. Shimizu, M., Hiramatsu, K. & Sawaki, N. Metalorganic vapor phase epitaxy growth of $(In_xGa_{1-x}N/GaN)n$ layered structures and reduction of indium droplets. *J. Cryst. Growth* **145**, 209–213 (1994).
7. Yoshimoto, N., Matsuoka, T., Sasaki, T. & Katsui, A. Photoluminescence of indium gallium nitride films grown at high temperature by metalorganic vapor phase epitaxy. *Appl. Phys. Lett.* **59**, 2251–2253 (1991).
8. Wu, J. *et al.* Small band gap bowing in $In_{1-x}Ga_xN$ alloys. *Appl. Phys. Lett.* **80**, 4741–4743 (2002).
9. Takahashi, N., Matsumoto, R., Koukitu, A. & Seki, H. Vapor-phase epitaxy of $In_xGa_{1-x}N$ using chloride sources. *J. Cryst. Growth* **189–190**, 37–41 (1998).
10. Davydov, V. Y. *et al.* Band gap of hexagonal InN and InGaN alloys. *Phys. Status Solidi B* **234**, 787–795 (2002).
11. Morkoc, H. *Nitride Semiconductors and Devices* (Springer, Berlin, 1999).
12. Perkins, N. R. *et al.* Growth of thick GaN films by halide vapor phase epitaxy. *Proc. Electrochem. Soc.* **96-5**, 336–341 (1996).
13. Lu, D. *et al.* Dynamic scaling of the growth process of GaN thin films deposited on sapphire substrates by HVPE. *Phys. Lett. A* **327**, 78–82 (2004).
14. Liliental-Weber, Z. *et al.* Compositional modulation in $In_xGa_{1-x}N$: TEM and X-ray studies. *J. Electron Microscopy* **54**, 243–250 (2005).
15. Kuykendall, T. *et al.* Crystallographic alignment of high-density gallium nitride nanowire arrays. *Nature Mater.* **3**, 524–528 (2004).
16. Sun, Y., Cho, Y.-H., Kim, H.-M. & Kang, T. W. High efficiency and brightness of blue light emission from dislocation-free InGaN/GaN quantum well nanorod arrays. *Appl. Phys. Lett.* **87**, 093115 (2005).
17. Ertekin, E., Greaney, P. A., Chrzan, D. C. & Sands, T. D. Equilibrium limits of coherency in strained nanowire heterostructures. *J. Appl. Phys.* **97**, 114325 (2005).
18. Fuhrmann, D. *et al.* Optimization scheme for the quantum efficiency of GaInN-based green light-emitting diodes. *Appl. Phys. Lett.* **88**, 071105 (2006).
19. Fuhrmann, D. *et al.* Optimizing the internal quantum efficiency of GaInN SQW structures for green light emitters. *Phys. Status Solidi C* **3**, 1966–1969 (2006).
20. Qian, F., Gradecak, S., Li, Y., Wen, C.-Y. & Lieber, C. M. Core/Multishell nanowire heterostructures as multicolor, high-efficiency light-emitting diodes. *Nano Lett.* **5**, 2287–2291 (2005).
21. Kim, H.-M. *et al.* High-brightness light emitting diodes using dislocation-free indium gallium nitride/gallium nitride multiquantum-well nanorod arrays. *Nano Lett.* **4**, 1059–1062 (2004).
22. Kim, H.-M. *et al.* Formation of InGaN nanorods with indium mole fractions by hydride vapor phase epitaxy. *Phys. Status Solidi B* **241**, 2802–2805 (2004).
23. Kumagai, Y., Takemoto, K., Hasegawa, T., Koukitu, A. & Seki, H. Thermodynamics on tri-halide vapor-phase epitaxy of GaN and $In_xGa_{1-x}N$ using $GaCl_3$ and $InCl_3$. *J. Cryst. Growth* **231**, 57–67 (2001).
24. Scholz, F. *et al.* Low pressure MOVPE of GaN and GaInN/GaN heterostructures. *J. Cryst. Growth* **170**, 321–324 (1997).
25. Doppalapudi, D., Basu, S. N., Ludwig, K. F. Jr & Moustakas, T. D. Phase separation and ordering in InGaN alloys grown by molecular beam epitaxy. *J. Appl. Phys.* **84**, 1389–1395 (1998).
26. Yang, B. *et al.* Structural and optical properties of GaN layers directly grown on 6H-SiC(0001) by plasma-assisted molecular beam epitaxy. *Mater. Sci. Forum* **264–268**, 1235–1238 (1998).
27. Snyder, R. L., Fiala, J. & Bunge, H. J. (eds) *Defect and Microstructure Analysis by Diffraction* (Int. Union Crystallogr. Monogr. Crystallogr., Vol. 10, Oxford Univ. Press, Oxford, 1999).
28. Mattila, T. & Zunger, A. Predicted bond length variation in wurtzite and zinc-blende InGaN and AlGaN alloys. *J. Appl. Phys.* **85**, 160–167 (1999).
29. Ho, I. H. & Stringfellow, G. B. Solid phase immiscibility in GaInN. *Appl. Phys. Lett.* **69**, 2701–2703 (1996).
30. Caetano, C., Teles, L. K., Marques, M., Dal Pino, A. Jr & Ferreira, L. G. Phase stability, chemical bonds, and gap bowing of $In_xGa_{1-x}N$ alloys: Comparison between cubic and wurtzite structures. *Phys. Rev. B* **74**, 045215 (2006).
31. Liliental-Weber, Z. *et al.* Relaxation of InGaN thin layers observed by X-ray and transmission electron microscopy studies. *J. Electron. Mater.* **30**, 439–444 (2001).
32. Stach, E. A. *et al.* Watching GaN nanowires grow. *Nano Lett.* **3**, 867–869 (2003).
33. Waltereit, P. *et al.* Nitride semiconductors free of electrostatic fields for efficient white light-emitting diodes. *Nature* **406**, 865–868 (2000).
34. Shubina, T. V. *et al.* Mie resonances, infrared emission, and the band gap of InN. *Phys. Rev. Lett.* **92**, 117407 (2004).
35. Wu, J. *et al.* Effects of the narrow band gap on the properties of InN. *Phys. Rev. B* **66**, 201403 (2002).

Acknowledgements

This work was supported in part by the US Department of Energy and DARPA-UPR. Work at the Lawrence Berkeley National Laboratory was supported by the Office of Science, Basic Energy Sciences, Division of Materials Science of the US Department of Energy. We thank T. Umbach, P. Pauzauskie and S.-Y. Bae for discussion, and the National Center for Electron Microscopy for the use of microscope facilities.

Correspondence and requests for materials should be addressed to P.Y.

Supplementary Information accompanies this paper on www.nature.com/naturematerials.

Reprints and permission information is available online at http://npg.nature.com/reprintsandpermissions/

© 2007 Nature Publishing Group